Back to Session Subjects

Detailed investigation of rotor blade tip vortex in hover condition by 2C and 3C-PIV

H. Richard[1], B. van der Wall[2]

[1]DLR, Institute of Aerodynamics and Flow Technology - Technical Flows -
Bunsenstraße 10, D-37073 Göttingen, Germany
e-mail: Hugues.Richard@dlr.de

[2]DLR, Institute of Flight Systems - Helicopter -
Lilienthalplatz 7, D-38108 Braunschweig, Germany
e-mail: Hugues.Richard@dlr.de

Key words: Blade tip vortex, hover, PIV

Abstract: In order to investigate the development of blade tip vortices under different rotor conditions like thrust and rotational speed, both two- and three-component PIV measurements were performed on a 40% Mach scaled Bo105 model rotor in hover condition. The vortices were traced from the trailing edge of the blade up to half a revolution behind the blade with azimuth steps between 1° to 10° and different spatial resolutions. In addition, a sequence of three-component measurements was performed just after the vortex creation at finer azimuth steps of 0.056° in order to generate a three-dimensional volumetric data set of the blade tip vortex. The influence of the PIV image analysis parameters on the vortex parameters derived - in particular sampling window size and window overlap - has been investigated. The measurements presented are part of the HOTIS (HOver TIp vortex Structure) project.

Nomenclature

Abbreviations

LDV	Laser Doppler Velocimetry
PIV	Particle Image Velocimetry
2C, 3C	Two, three component

Symbols

a_∞	speed of sound, m/s
c	chord of the blade, m
C_T	thrust coefficient, $= T/(\rho\pi\Omega^2R^4)$
L_m	measurement length, m
M_H	hover tip Mach number, $= \Omega R/a_\infty$
N_b	number of blades
r	radial coordinate, m
r_c	core radius, m
R	rotor radius, m
Re_v	vortex Reynolds number, $= \Gamma_v/\nu$
T	thrust, N
u,v,w	velocity components, m/s
x,y,z	coordinates, m
V_0	peak axial velocity, m/s
V_θ	swirl velocity, m/s
Γ	circulation, $= 2\pi r V_\theta$, m^2/s
Γ_v	circulation at large distance, m^2/s
ν	kinematic viscosity, m^2/s
ρ	air density, kg/m^3
σ	rotor solidity, $N_b c/\pi R$
Ψ_b	azimuthal blade position, based on quarter chord line, deg
Ψ_v	vortex age, based on quarter chord line, deg
$\omega_{x,y,z}$	vorticity components, rad/s
Ω	rotational speed of the rotor, rad/s

1 INTRODUCTION

Within the last decade a large number of experimental investigations were performed in order to better understand and to model the development of rotor blade tip vortices. Most of these studies were done in hovering condition, because the flow field is azimuthally axisymmetric under this condition, the vortices are convected below the rotor plane and are isolated in early stage in comparison to forward or descent flight where the vortices are entrained downstream and might interact with blade wake, other vortices and/or with the following blades. Blade vortex interactions are responsible for the so-called blade-vortex interaction noise. While earlier velocity measurements were obtained using intrusive techniques such as hot-wires, more recent flow measurements rely exclusively on optical techniques, mainly Laser Doppler Velocimetry (LDV) [1], [2] and Particle Image Velocimetry (PIV) [3], [4].

Within the HOTIS (HOver TIp vortex Structure) project velocity field measurements were conducted using two-component (2C) and three-component (3C) PIV on a four-bladed rotor in hover condition in ground effect inside the rotor preparation hall at DLR Braunschweig. In order to investigate the aging process of the blade tip vortex and the influence of the rotor parameters on the vortex characteristics measurements were made at different vortex ages from Ψ_v=3.6° to 152.6° with respect to quarter chord line (=1° to 150° behind the trailing edge) for several rotor parameters: rotation speed (200, 540 and 1041rpm) and thrust (from 0N to 3500N). The blade tip vortex was measured with different spatial resolutions: low and very high spatial resolution in case of 2C-PIV measurements and with high spatial resolution for 3C-PIV. The spatial resolution, defined by the field of view and the size of the interrogation window, is an important parameter when looking for vortex properties such as maximum swirl velocity or core radius [3].

In addition to these measurements, 3C measurements were performed for vortex ages between Ψ_v=6° and 9.6° (with respect to quarter chord line) using very fine age increments of 0.056° in order to generate an averaged volumetrically resolved velocity data set of the vortex.

2 EXPERIMENTAL SETUP

2.1 Rotor model

The rotor is a 40%, dynamically and Mach-scaled Bo105 main rotor with a radius of R=2m. It is composed by four hingeless blades that have a pre-cone of 2.5° at the hub, rectangular plan form with chord length of c=0.121m, -8°/R linear twist and a solidity of σ=0.077. The model was driven by a hydraulic motor and was installed in the center of the 12m*12m*8m rotor testing hall of DLR Braunschweig as shown on
Fig. 1.

The rotor was operated in ground effect – the hub center located 2.87m (1.437R) above the ground – at different rotation speeds of 200, 540 and 1041rpm, corresponding to tip Mach numbers of M_H=0.122, 0.329 and 0.633, and with different thrust coefficients varying from C_T/σ=0 to 0.072. Due to the closed hall, recirculation existed and generated an inherently unsteady flow field.

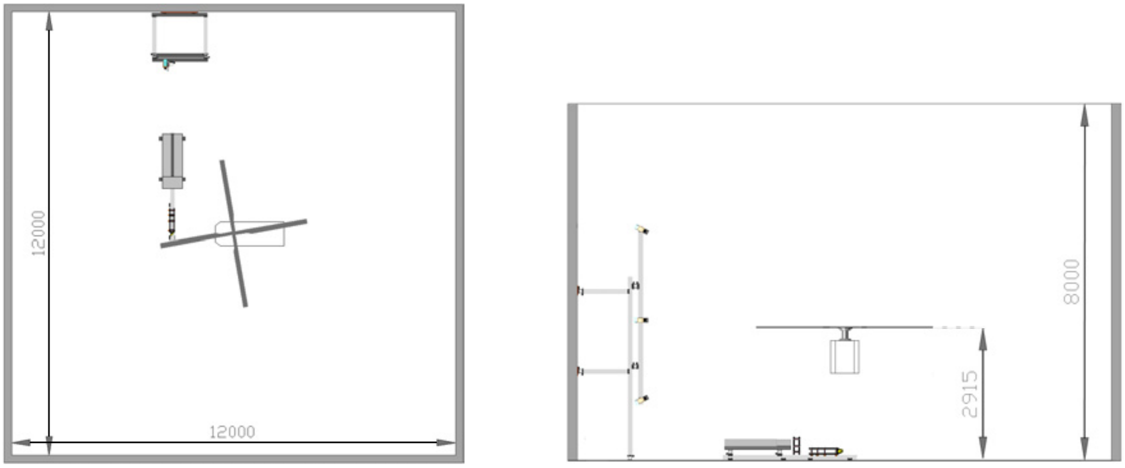

Fig. 1. Sketch of the DLR-Braunschweig rotor testing hall.

2.2 PIV

The illumination source of the PIV setup consisted of a double oscillator, frequency-doubled Nd:YAG laser (320mJ/pulse at 532nm) and light sheet forming optics which were bolted to the ground below the rotor. The light sheet was oriented vertically upward and parallel to the trailing edge of the rotor blade when the blade was at 0° azimuthal angle and had a waist thickness of 1-2mm at the measurement plane and a width of around 30cm. According to the blade geometry, the azimuth of the trailing edge is 2.6° behind the quarter chord line at the trailing edge. Three thermo-electrically cooled CCD-cameras (1 PCO Sensicam, 1280 x 1024 pixels and 2 PCO Sensicam QE, 1360 x 1076 pixels) were used: one camera for 2C PIV and for recording the position of the blade tip and the two other cameras equipped with Scheimpflug adapter in stereo arrangement for 3C PIV. They were mounted on a support structure consisting of X-95 rails which was bolted to the wall of the testing hall. Each camera was connected through fiber optic cable to acquisition computers located outside the hall.

The complete PIV setup is shown on Fig. 2. The camera support can be seen on the left hand side of the figures. The cameras were located at 4.5m from the rotor hub and the stereo cameras were mounted with a stereo viewing angle of 47°. Laser and camera were synchronized according to the one per revolution signal given by the reference blade of the rotor. This signal was delayed using a phase-shifter [5] in order to measure at a desired blade azimuth angle. The separation time between the two laser pulses was between 2 to 18µs according to the field of view and to the flow field.

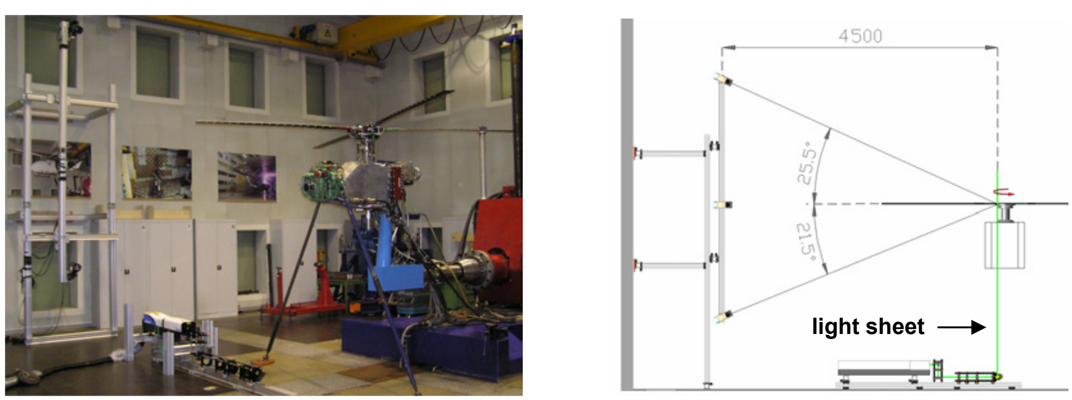

Fig. 2. Photo and sketch of the PIV setup and of the rotor model.

2.3 Blade tip position

Prior to the PIV measurement, the cameras were calibrated and the location of the blade tip at rest was measured on the calibration grid. Then this location was recorded using the middle camera, equipped with 85mm lens, for all the different rotor settings in order to correct the origin of the vector fields. For every rotor configuration, 50 images of the blade tip were recorded. Fig. 3 shows the position of the blade tip at rest and two instantaneous recordings for $C_T/\sigma=0$ (T=0N) and 0.045 (T=2500N) at $M_H=0.633$ ($\Omega=109$rad/s.)

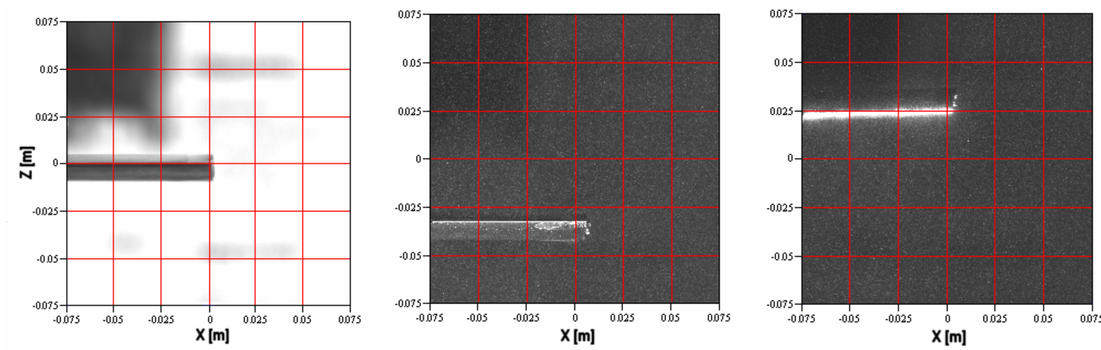

Fig. 3. Instantaneous blade tip position measurement at rest and for $C_T/\sigma=0$ (T=0N) and $C_T/\sigma= 0.045$ (T=2500N) at $M_H=0.633$ ($\Omega=109$rad/s).

Fig. 4 shows the locations of the tip of the blade relative to its location at rest for the different thrust and for the different rotational speed.

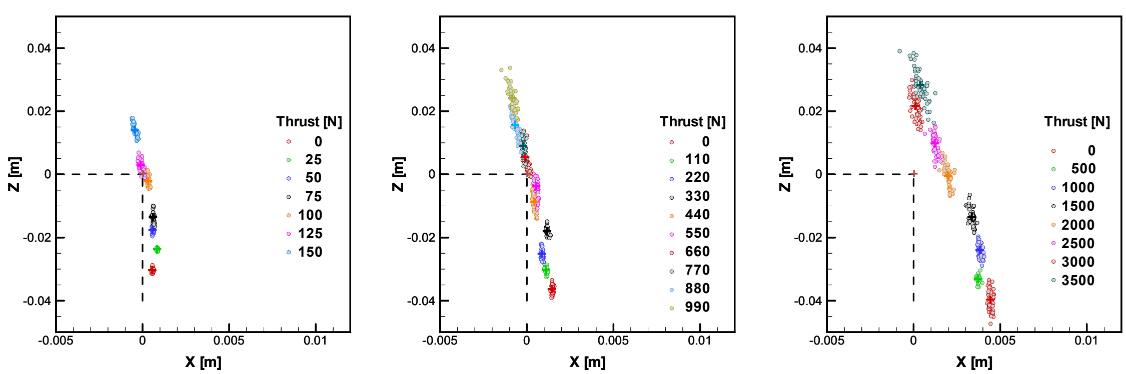

Fig. 4. Blade tip position for the different thrust settings at $M_H= 0.122$, 0.329 and 0.633.

The origin of the coordinate system is located at the blade tip at rest, i.e. at X=Y=Z=0m, whereas the hub center is located at X=-2m, Y=0.09m and Z=-0.04m. It has a cone angle of 2.5deg at the root and outside the bends down due to its weight and gravity forces. For tip Mach number of 0.633, during rotation and zero thrust, the blade tip is located about 4.3mm outside and 40mm lower due to centrifugal forces that stretch the blade and confine most of the bending to the blade root area. With increasing thrust the blade tip rises by about 70mm (approximately 2deg flap angle) at $C_T/\sigma=0.063$ (T=3500N, which is the scaled representative for a 2200kg Bo105) and moves little inboard as expected. The vertical scatter is mainly caused by dynamic blade flapping response to the unsteady aerodynamic environment including circulation and turbulence, and less by some vibratory motion of the test rig. Thus, the blade tip position is slightly different from revolution to revolution.

3 PIV EVALUATION AND POST-PROCESSING

3.1 Processing

Based on the calibration grid the images recorded by the stereo camera were first dewarped, and then misalignment correction was applied. This correction is necessary to insure that the fields of view from the two cameras exactly coincide and consists of a correlation analysis on the images acquired at the same instant of time from the two views (upper and lower camera view). The resulting vector map corresponds to the misalignment between the two camera views mainly due to the fact that it is not possible to perfectly align the calibration grid within the light sheet. This misalignment was found to be equal to 100px which represents few millimeters in the image plane. The vector map is then used to correct the original dewarp coefficients which are finally used to dewarp the raw PIV images.

All the images obtained during the measurement were first pre-processed using high pass filter, then binarization filter and finally anti-alias filter in order to increase the signal to noise ratio. Multi-grid algorithm was applied to process the image which consists of a pyramid approach by starting off with large interrogation windows on a coarse grid and refining the windows and grid with each pass. A window size of 64x64px was used as initial sampling window and for most of the recording, 24x24px as final window size with Whittaker reconstruction peak fit and 75% overlap. All the processing was done using PIVview software. More details about the software and algorithm can be found in [7] and [8].

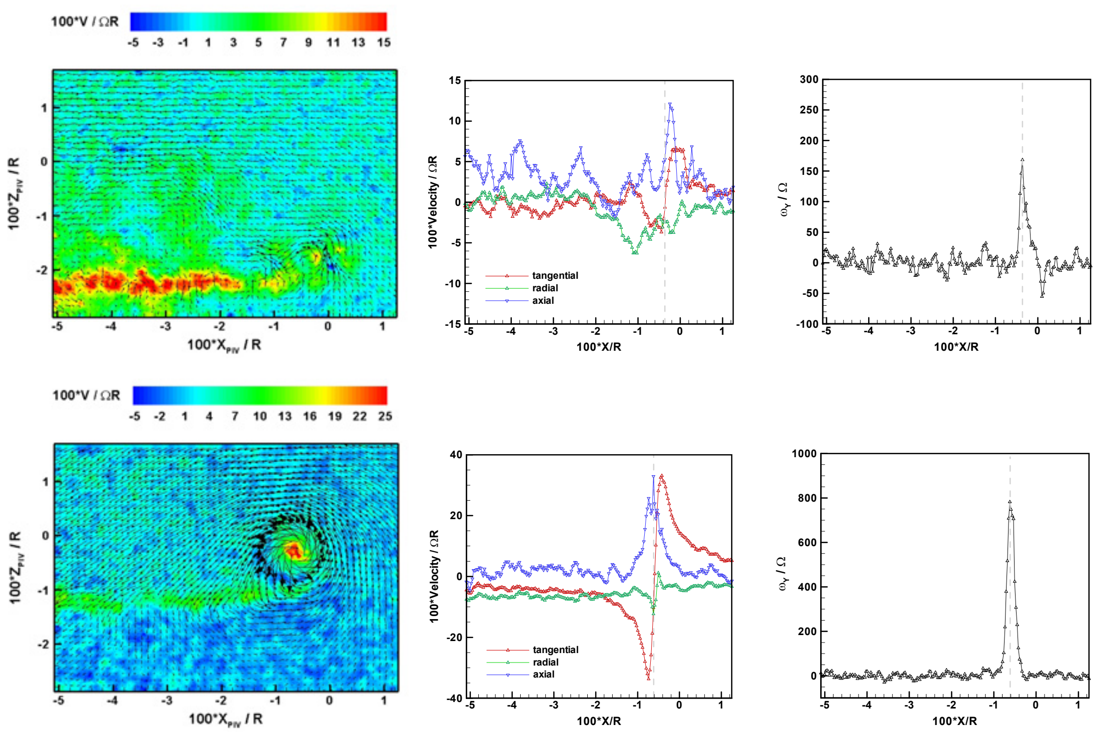

Fig. 5. Normalized instantaneous velocity and their velocity and vorticity profiles, Ψ_v=7.6°, M_H=0.633, for C_T /σ=0.009 (T=500N) (top) and C_T /σ=0.036 (T=2000N) (bottom).

Fig. 5 shows two examples of instantaneous 3C results, out-of-plane component color coded, and their horizontal velocity and vorticity profiles obtained at Ψ_v=7.6° for M_H=0.633 for two different thrust: C_T /σ=0.009 (top) and C_T /σ=0.036 (bottom). One can clearly identified the vortex sheet trailed behind the blade as well as the blade tip vortex for the higher thrust. In case of C_T/σ=0.009 thrust coefficient, the blade tip vortex is much weaker and thus more difficult to localize.

Once the vector field obtained, automatic outliers detection procedure is applied. It consists of a scan of the vector fields and a computation of the vector difference between each vector and its eight neighbors. If the magnitude of this difference exceeds a specified threshold (defined according to the flow field and the field of view), the tag for this vector is increased by one. If the total tag value for a specific vector exceeds 5, then it is labeled as a spurious vector. After being detected, the outliers are removed and replaced using a bi-linear interpolation involving the surrounding valid neighbors. In cases where a number of immediate neighbors are labeled as outliers, a Gaussian weighted scheme is used.

3.2 Spatial resolution

The primary aim of these measurements was to gain a better understanding of the development of the blade tip vortex, especially in its early stages of development. The velocity vector fields are used to extract vortex characteristics such as the maximum swirl velocity, the core radius or the peak of vorticity. Prior to the full processing of the PIV image, the influence of the PIV interrogation window size and overlap on these characteristics was investigated.

Sampling window size: One of the most important PIV parameters is the size of the interrogation or sampling window which, in terms of other measurement techniques, defines the probe volume.

WS [px]	Lm/c	r_c/c	Lm/r_c	$V_\theta/\Omega R$	$V_0/\Omega R$	ω_{y0}/Ω
16	0.0124	0.021	0.59	0.31	0.16	992
24	0.0191	0.0221	0.87	0.31	0.14	990
32	0.0255	0.0262	0.97	0.30	0.14	895
48	0.0382	0.0287	1.33	0.29	0.13	884
64	0.051	0.035	1.46	0.25	0.10	700

Table 1 Comparison of vortex characteristics extracted from 3C averaged result processed with different interrogation window sizes (Ψ_v=7.6°, M_H=0.633, C_T/σ=0.036).

In table 1 vortex characteristics extracted from averaged results (Ψ_v=7.6°, M_H=0.633 and C_T/σ=0.036) obtained using different cross-correlation windows size with a constant window overlap of 6px are listed.

The decrease of window size results in an increase of maximum swirl velocity, axial velocity and a decrease of vortex radius. The size of the interrogation window should be as small as possible but it is limited by the experimental parameters like seeding distribution, in-plane lost in pair (mainly compensate by multi-grid algorithm), out-of-plane lost of pair, low image intensity or image background noise [9][10][11][12]. Most of these parameters can be optimized by adapting the pulse separation time, light sheet width or light sheet thickness according to the flow field. Nevertheless the parameter which still limits the decrease of the window size is the particle density inside the vortex core. Indeed blade tip vortex in hover condition are characterized by a low seeding density inside the vortex core (Fig. 14(a)) due to the centrifugal force which drives the seeding particles outwards from the vortex center. To be statistically meaning-

ful, the cross-correlation requires at least 10 particle images per interrogation window which is sometimes difficult in the vortex core. In order to decrease this void, smaller particles can be used but it has to be kept in mind that, according to the Mie theory, a decrease of particle diameter requires a quadratic increase of laser energy in order to keep the amount of light scattered by the particles constant. The use of too small window size results in outliers in the vortex core which should be removed and interpolated and can not be used for analysis like the 16*16px window size presented in the table 1 where most of the vector inside the core were interpolated as shown in
Fig. 6.

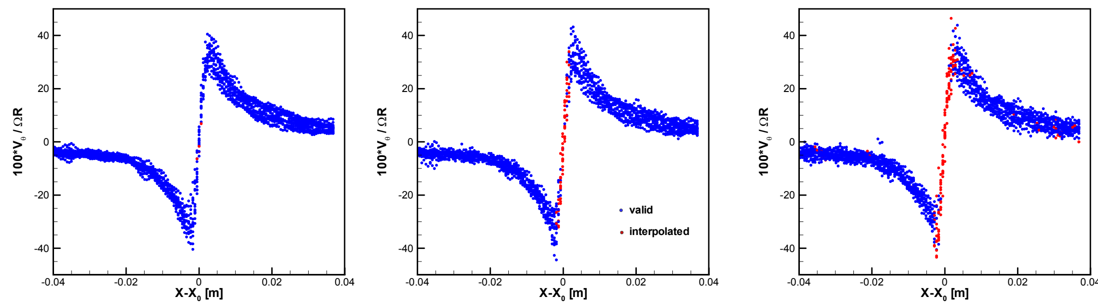

24x24px 16x16px 12x12px

Fig. 6 Tangential velocity profiles (blue: valid data, red: interpolated) (Ψ_v=7.6°, M_H=0.633, C_T/σ=0.036).

In
Fig. 6, some instantaneous tangential profiles are plotted with interpolated points colored in red. As it can be seen the number of outliers in the vortex core is increasing as the window size is decreasing from the vortex center towards the outer part of the vortex following the particle density. In this paper, all the PIV images were processed using 24x24px windows because it allows over the complete vortex age and rotor parameters to keep a low number of outliers.

Sampling window overlap: The second parameter study was done on the sampling window overlap value. This value defines the interrogation interval (sample points) and is very often set by default to 50% of the window size: the neighbouring interrogation areas sample 50% of the same particles image.

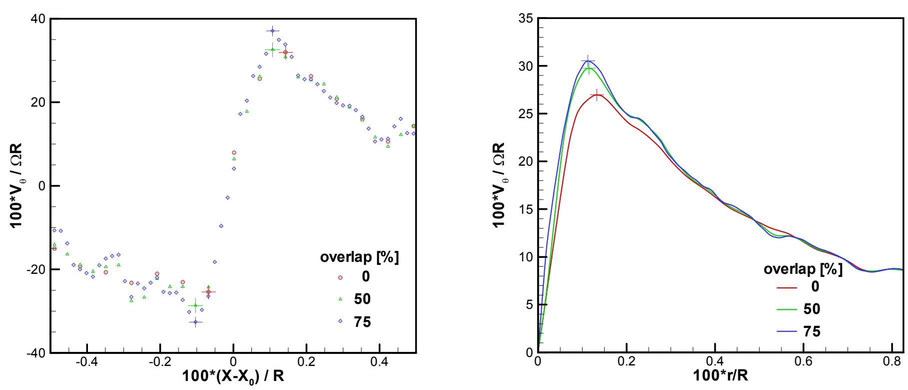

Fig. 7 Instantaneous tangential velocity profiles (Ψ_v=7.6°, M_H=0.328 and C_T/σ=0.036).

Fig. 7 shows horizontal and averaged tangential velocity profile extracted from an instantaneous result processed with 0%, 50% and 75% overlap to highlight that this parameter should not be neglected while looking for information such as core radius or maximum swirl velocity.

Numerical investigations of the effect of correlation window overlap on vortex characteristics (maximum swirl velocity and core radius) were performed in [3] using a Vatistas model [20]. The same investigation was reproduced using the previously mentioned instantaneous PIV image of Fig. 7 (Ψ_v=7.6°, M_H=0.328 and C_T/σ=0.036).

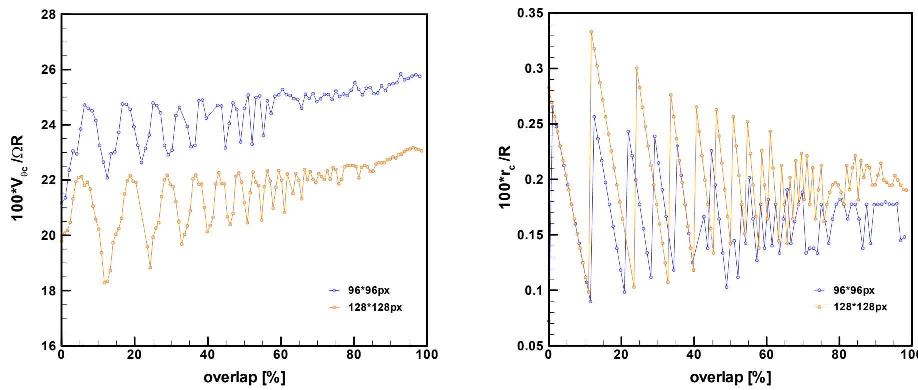

Fig. 8. Maximum tangential velocity and core radius versus overlap (Ψ_v=7.6°, M_H=0.328 and C_T/σ=0.036).

First this image was processed with 96x96px and 128x128px windows sizes with overlap between 2px (98% overlap) to the window size value (0% overlap) in X direction whereas the overlap in Y direction was kept constant at 50% of the window size.
Fig. 8 shows the maximum tangential (swirl) velocity and core radius extracted from the horizontal velocity profile (one dimensional analysis).
The curves obtained are in good agreement with the numerical simulation mentioned before. They converge to different values depending of the window size and are oscillating with values which are decreasing when the overlap increases. The swirl velocity values are always equal or below the value obtained with the maximum sampling whereas the core radius oscillates around it. Maximum swirl velocity is reached when the center point of an interrogation window falls onto the maximum in the velocity profile which has an increased probability as the overlap is increased.

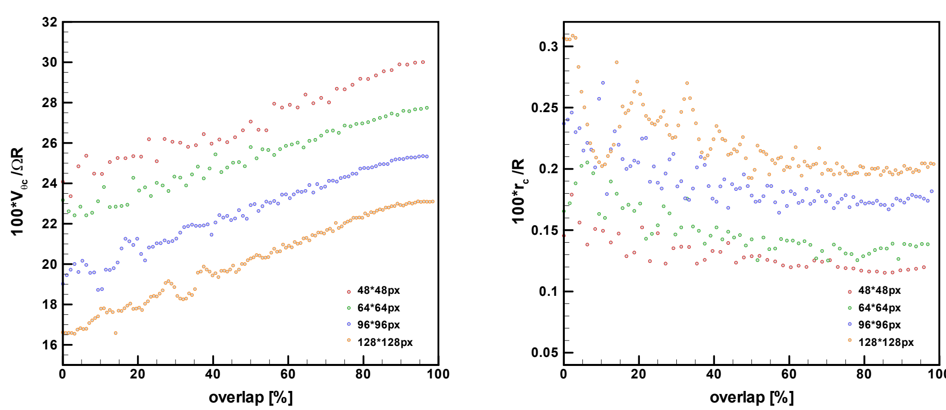

Fig. 9. Maximum tangential velocity and core radius versus overlap (Ψ_v=7.6°, M_H=0.328 and C_T/σ=0.036).

In a second step the same image was processed using window sizes of 48, 64, 96, and 128px size with overlap between 2px and the window size value. The maximum swirl velocity and core radius were computed by averaging circularly the tangential velocity profile over r (two dimensional analysis), the radial distance from the vortex center. This radial averaging method is known to be more robust [13]. The curves obtained are presented on Fig. 9. The effect of the window size is still noticeable but the curves are smoother and the oscillations which were observed in
Fig. 8 are nearly completely damped. This investigation shows that the overlap parameter can play an important role when looking for vortex characteristics and - in order to avoid random effect - an overlap as large as possible should be used in order to avoid these sampling artifacts.

3.3 Conditional average and post-processing

In order to retain vortex characteristics, e.g. core radius or maximum swirl velocity, simple (ensemble) average can not be used because of vortex wander. Due to flow instability and to non perfect periodicity of the rotor behavior, e.g. the position of the blade tip, the location of the vortex is changing from one image to the other which implies that conditional averaging is mandatory in order to avoid artificial smoothing.

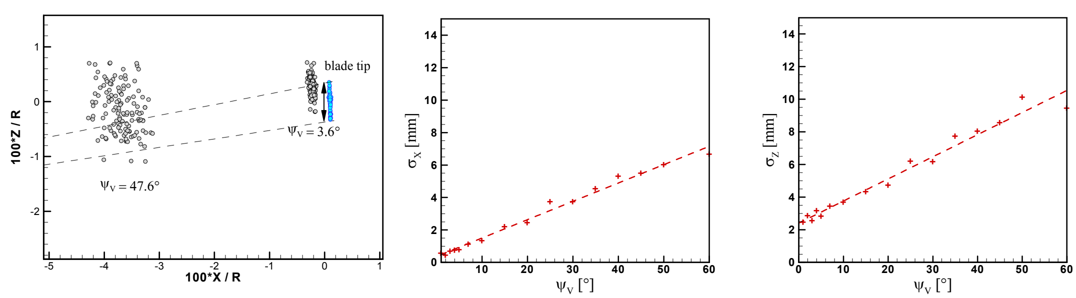

Fig. 10 Vortex position for Ψ_v=3.6° and Ψ_v=47.6° and hor. and vertical standard deviation (M_H=0.633 and C_T/σ=0.036).

Fig. 10 shows, on the left hand side, the location of the vortices for two different vortex ages: Ψ_v=3.6° and Ψ_v=47.6° relative to the blade tip position and the standard deviation of the vortex position in function of the age. As it can be seen the scatter of vortex position in space observed for Ψ_v=3.6° is mainly due to the non periodicity of the blade tip position. Indeed the amplitude of the blade tip displacement for this configuration represents more than 75% of the amplitude observed here. The radial and vertical scatter increases linearly with age till the next blade passage. Many methods have been described in the literature to detect coherent structures and in particular vortices [3][13]. In the present article, the conditional average is done after locating the vortex center using wavelet detection method as described in [21]. Once the center detected, they are shifted to a common point before performing the average.

3.4 3D results

As introduced before, in addition to azimuth steps of 1° to 10°, sequences of 3C measurements were performed with vortex age increments of about $\Delta\Psi$=0.056° (=1.95mm at the blade tip) for

vortex ages from Ψ_v=6° to 9.6° for different rotor conditions. These small increments allow reconstructing a 3D volume of the vortex due to the azimuthally axisymmetric behavior of the flow field.
Fig. 11 shows the different planes measured for a vortex age between Ψ_v=3.6° and 52.6° and the 65 planes used to generate the volume, the azimuthal space is similar to the in-plane resolution within each image and thus the flow gradients are of the same accuracy as those computed from the single flow field itself.

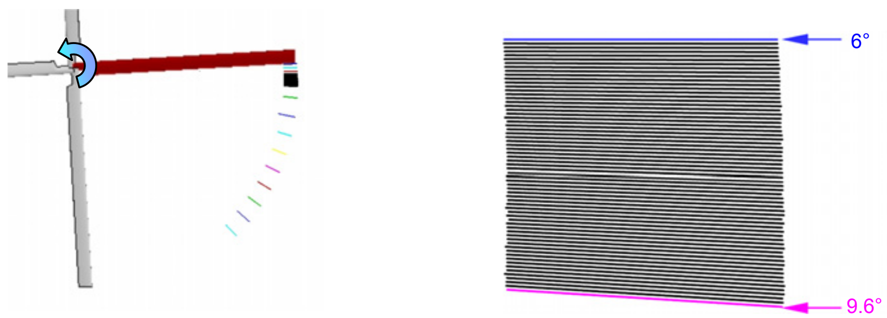

Fig. 11. 3C-PIV planes and zoom view of the volume plane.

The resulting volume allows the computation of the two missing components of the vorticity vector (ω_x and ω_z), based on out-of-plane derivatives of u, v and w.

$$\omega_x = \frac{\partial w}{\partial y} - \frac{\partial v}{\partial z} \qquad \omega_y = \frac{\partial u}{\partial z} - \frac{\partial w}{\partial x} \qquad \omega_z = \frac{\partial v}{\partial x} - \frac{\partial u}{\partial y}$$

The reconstruction of the volume can only be done using conditionally averaged results because every plane forming the volume was recorded at different instants of time. After conditional averaging, the orientation of each plane was corrected as shown in Fig. 11, in order to take the step angle into account. Fig. 12 shows the volume after merging all the 3C PIV vector fields, with the contour of the three vorticity components: (a): ω_x, (b): ω_y and (c): ω_z. The volume obtained contains around 3 millions points.

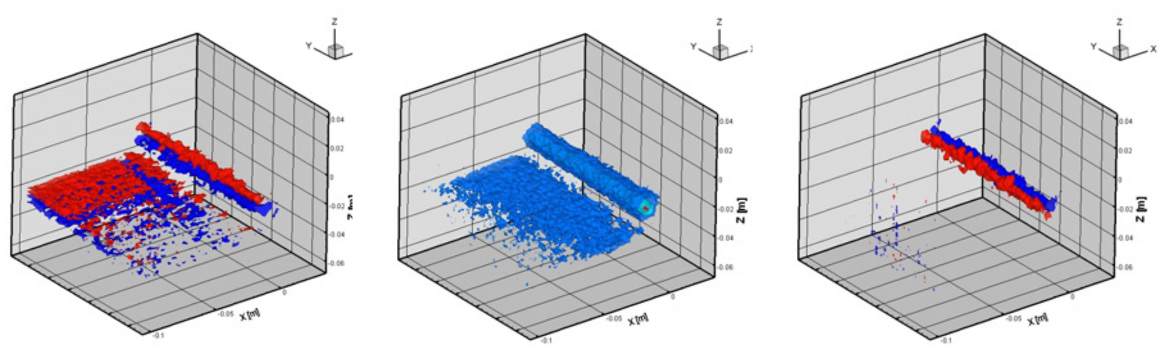

(a): ω_x (b): ω_y (c): ω_z

Fig. 12. Three components of vorticity (6° < Ψ_v <9.6°, M_H=0.633 and C_T/σ=0.036).

Fig. 13 shows the contour plot of the out-of-plane component on the left hand side and of the magnitude of the three vorticity components on the right hand side. The vortex tube as well as the blade wake is clearly visible on these two graphs.

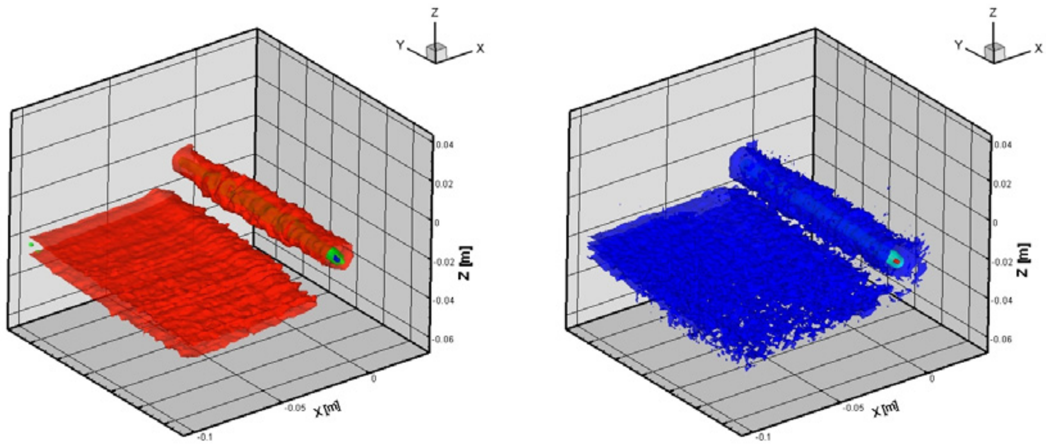

(a):V component (b): $||\omega||$

Fig. 13. Volume reconstruction of (a): the out-of-plane component, (b) the vorticity magnitude ($6° < \Psi_v < 9.6°$, M_H=0.633 and C_T/σ=0.036).

4 RESULTS AND DISCUSSION

4.1 Vortex flight path

Fig. 14 shows one instantaneous PIV image (left hand side) and the corresponding vorticity and velocity fields (middle) obtained with the large field of view camera (85mm lens) where the vortex generated by each blade can be clearly seen ($\Psi_v \approx$ 3°, 93°, 183° and 273°). Due to the centrifugal force, the particles are driven outwards from the vortex center giving it the appearance of a "void" which increases diameter with age.

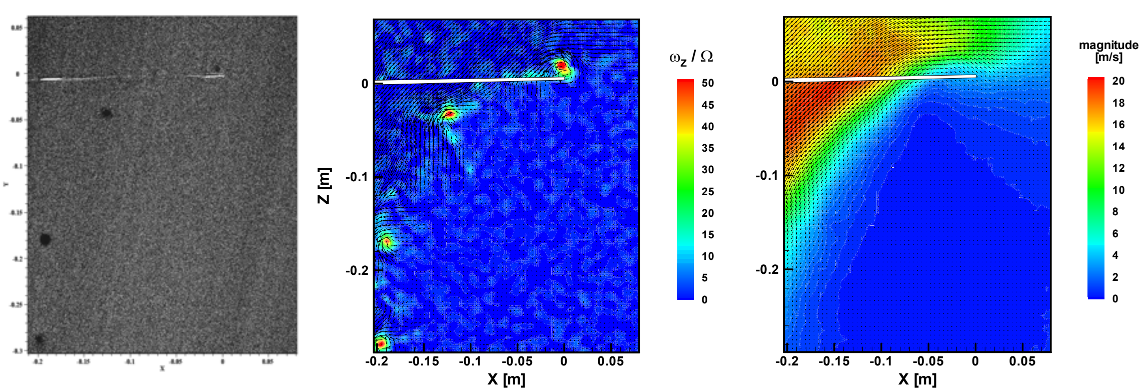

(a) (b) (c)

Fig. 14 (a): Instantaneous PIV image (large field of view), (b): its corresponding vector and vorticity field, (c): average vector and magnitude field (over 2000 samples in free run mode) (M_H=0.633 and C_T/σ=0.036).

The simple averaged velocity field, shown in Fig. 14 (right hand side) was computed using 2000 recording which were not triggered with the rotor (free run mode). It allows estimating the vortex path that is characteristic of a hovering rotor. The contraction of the wake boundary is clearly visible with a mean velocity field outside this region close to zero.

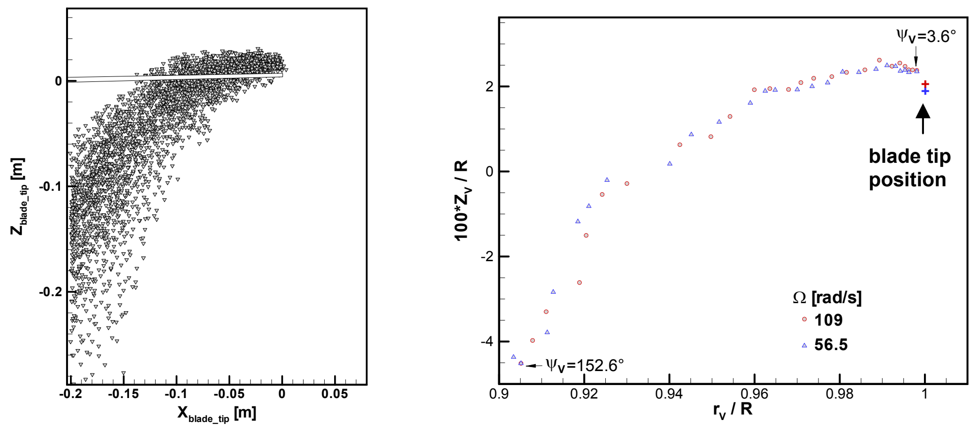

(a) (b)

Fig. 15 (a): vortex position (large field of view) (M_H=0.633), (b): vortex flight path (C_T/σ=0.036).

Fig. 15 shows on the left hand side the instantaneous vortex center location based on the large field of view PIV results and on the right hand side the averaged vortex position obtained with the 3C PIV system for the main tip speeds, M_H=0.328 and 0.633. The increase of scatter of vortex positions in space mentioned before can be clearly seen on Fig. 15 (a). The vortices are released few millimeters inboard of the upper surface of the blades and are convected inboard and downward along the slipstream visible on the velocity magnitude field, Fig. 14 (right hand side).

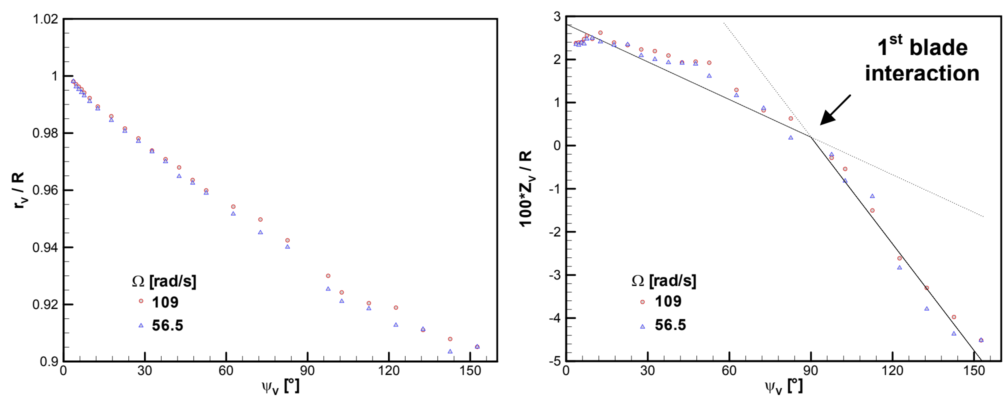

Fig. 16. Vortex radial and vertical position (M_H=0.328 and M_H=0.633, C_T/σ=0.036).

Fig. 16 shows that from its creation to an age of around 50° the vortices are mainly convected inboard on the upper surface of the blade. After the 1st blade passage (at Ψ_v=90°), the vertical convection is about 3 times as large which is consistent with other hover wake measurements.

4.2 Aging process

The development of swirl velocity, core radius, vorticity peak and axial velocity extracted from the averaged vector field are presented on Fig. 17 and Fig. 18 for M_H=0.328 and 0.633 and a constant rotor loading of C_T/σ=0.036. As shown, the swirl velocity is decreasing with age from 43m/s (38% of the blade tip speed) at Ψ_v=3.6° to 10m/s at Ψ_v=152.6° for M_H=0.328 and from 75m/s (35% of the blade tip speed) to 19m/s for M_H=0.633.

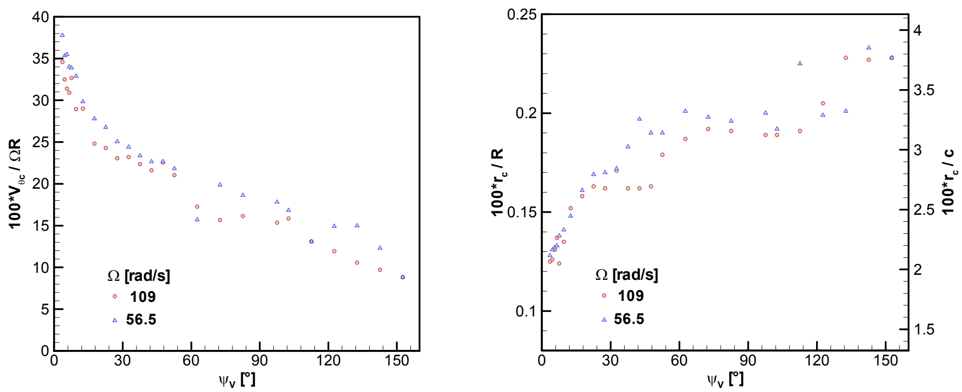

Fig. 17. Development of swirl velocity and core radius (M_H=0.328 and M_H=0.633, C_T/σ=0.036).

In parallel the core radius increase from 2.5mm up to 4.6mm which represent respectively 2.1% and 3.8% of the blade chord which is in good agreement with other measurement performed on rotor operating in hover [4].

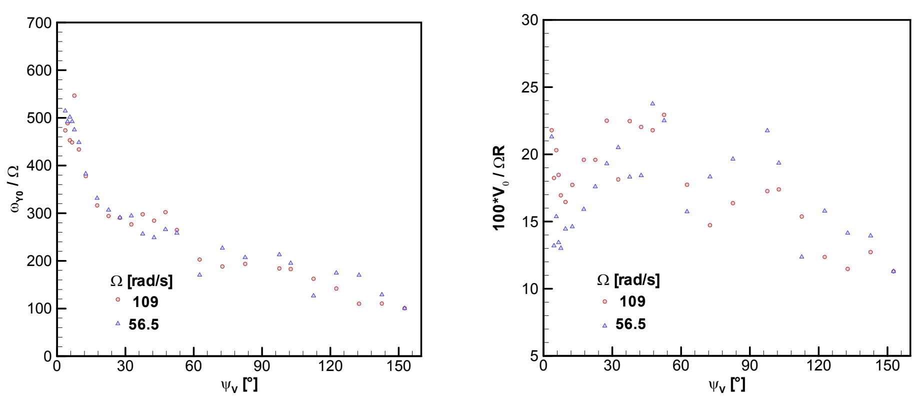

Fig. 18 Development of peak vorticity and axial velocity (M_H=0.328 and M_H=0.633, C_T/σ=0.036).

Within 150° the peak of vorticity is decreasing by a factor of 5, as plotted in Fig. 18, whereas the axial velocity in the center of the vortex is directed towards the blade and is not quickly dropping rather than staying with values between 15 to 25% of the tip speed. This is very likely due to the fact that the resolution of the stereo PIV system used is not high enough to resolve properly the young vortices with ages less than Ψ_v=45°. The non-dimensional vortex parameters like swirl velocity and core radius are independent of the tip speed.

4.3 Thrust variation

Fig. 19 and Fig. 20 show the variation of vortex characteristics as function of rotor loading for Ψ_v=7.6° and M_H=0.328 and 0.633.

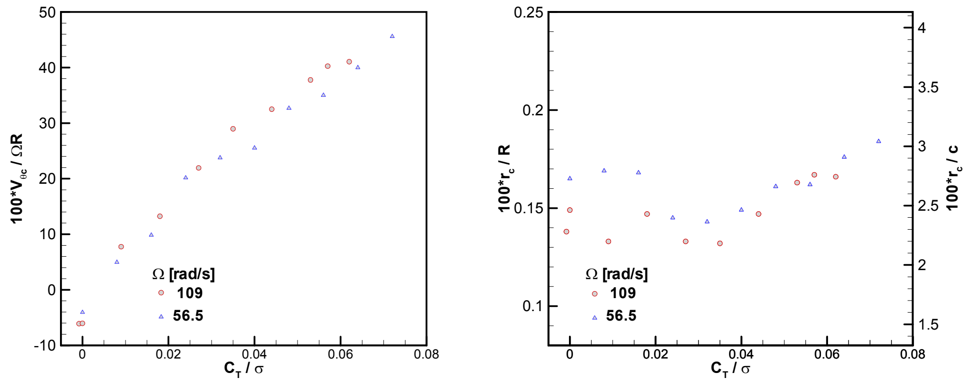

Fig. 19 Variation of swirl velocity and core radius for Ψ_v=7.6° as function of rotor loading (M_H=0.328 and M_H=0.633).

The maximum swirl velocity is increasing with the rotor loading and like the aging process seems to be independent from the tip speed and the core radius seems also to be independent of the thrust at least for low thrust values. For C_T/σ=0, we can observe a negative swirl velocity which is due to the linear twist of the rotor blade which requires negative loading at the tip for zero thrust to counter-balance the lift in the inboard area.

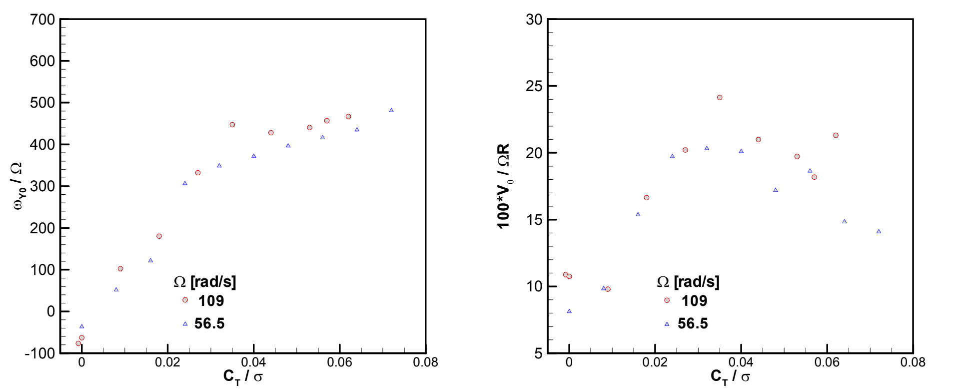

Fig. 20 Variation of peak vorticity and axial velocity for Ψ_v=7.6° in function of rotor loading (M_H=0.328 and M_H=0.633).

like the swirl velocity, the vorticity peak in the vortex center is increasing with the loading with negative values for zero thrust: the vortex is rotating in opposite direction compared to higher thrust, which is due to negative loading at the tip as explained before. For C_T/σ=0, the axial velocity value does not reach zero value because the axial velocity is now dominated by the shear layer trailed behind the blade.

5 CONCLUSION

In this paper, the HOTIS (HOver TIp vortex Structure) test performed in the rotor testing hall of DLR Braunschweig using 2C and 3C-PIV was described. This test was performed with a 40% Mach scaled model rotor of the Bo105 in hover condition at different RPM and thrust. The blade tip vortices were traced from their creation up to half revolution with small age increments. A parametric study of the two main PIV parameters - the correlation window size and the overlap - was done. It shows that the overlap parameter which is often set by default to 50% of the window should be as large as possible in order to avoid random effects and to improve the accuracy of vortex characteristics which can be extracted from the result. Preliminary results show that in order to resolve properly the vortex characteristics and particularly the core radius of young vortices, higher resolution than the one used for the stereo measurement is mandatory like the one used for the 2C very high resolution.

A three-dimensional reconstruction of the blade tip vortex has been applied for vortex ages between Ψ_v=6° and 9.6° using a very fine age increment step of $\Delta\Psi_v$=0.056°. This volume reconstruction allows computing all the differential quantities which are not possible to obtain with normal 3C-PIV results and to visualize the vortex tube as well as the wake of the blade. A first post-processing and analysis shows that the vortex characteristics - swirl velocity, core radius and axial velocity - seem to be independent of the blade tip speed at least in the range measured during the test ($0.122 \leq M_H \leq 0.633$).

6 REFERENCES

[1] Boutier A, Lefevre J, Micheli F (1996) Analysis of Helicopter Blade Vortex Structure by Laser Velocimetry. Exp. In Fluids **21**: 33-42

[2] Raffel M, Seelhorst U, Willert C (1998) Vortical Flow Structures at a Helicopter Rotor Model Measured by LDV and PIV. Aeronautical Journal **104** No. 1014: 221-227

[3] van der Wall BG, Richard H (2005) Analysis methodology for 3C PIV data. Proc: 31st European Rotorcraft Forum, Florence, Italy

[4] Martin PB, Leishman JG, Pugliese GJ, Anderson SL (2000) Stereoscopic PIV measurements in the wake of a hovering rotor. Proc. 56th Annual Forum of the American Helicopter Society, Virginia Beach, USA

[5] Stasicki B, Ehrenfried K, Dieterle L, Ludwikowski K, Raffel M (2001) Advanced synchronization techniques for complex flow field investigations by means of PIV. Proc: 4th Int. Symp. On Particle Image Velocimetry, Göttingen, Germany.

[6] Raffel M, Richard H, Ehrenfried K, van der Wall BG, Burley CL, Beaumier P, McAlister K, Pengel K (2004) Recording and Evaluation Methods of PIV investigations on a Helicopter Rotor Model. Exp. In Fluids **36**: 146-156

[7] 'PIVview2C/3C User Manual', http://www.pivtec.com

[8] Stanislas M, Okamoto K, Kähler CJ, Westerweel J (2005) Main results of the Second International PIV Challenge. Exp. In Fluids **39**: 170-191

[9] Willert CE, Gharib M (1991) Digital Particle Image Velocimetry. Exp. In Fluids **10**: 181-193

[10] Keane RD, Adrian RJ (1992) Theory of cross-correlation of PIV images. Applied Scientific Research **49**: 191-215

[11] Westerweel J, Dabiri D, Gharib M (1997) The effect of a Discrete Window Offset on the Accuracy of Cross-Correlation Analysis of Digital PIV Recordings. Exp. In Fluids **23**: 20-28

[12] Prasad AK, Adrian RJ, Landreth CC, Offutt PW (1992) Effect of Resolution on the Speed and Accuracy of Particle Image Velocimetry Interrogation. Exp. In Fluids **13**: 105-116

[13] Burley CL, Brooks TF, van der Wall BG, Richard H, Raffel M, Beaumier P, Delrieux Y, Lim JW, Yu YH, Tung C, Pengel K, Mercker E (2002) Rotor wake vortex definition and validation from 3-C PIV HART II study. Proc: 28th European Rotorcraft Forum, Bristol, England

[14] Jeong J, Hussain H (1995) On the identification of a vortex. Journal of Fluid. Mech. **285**: 69-94,

[15] McAlister KW (2004) Rotor wake development during the first revolution. Journal of the American Helicopter Society: **49** No. 4

[16] van der Wall BG, Junker B, Yu YH, Burley CL, Brooks TF, Tung C, Raffel M, Richard H, Wagner W, Mercker E, Pengel K, Holthusen H, Beaumier P, Delrieux Y (2002) The HART II test in the LLF of the DNW - a major step towards rotor wake understanding. Proc: 28th European Rotorcraft Forum, Bristol, England

[17] Vatistas GH, Kozel V, Mih WC (1991) A simpler model for concentrated vortices. Exp. In Fluids **11**:73-76

[18] Schram C, Riethmuller ML (2001) Vortex ring evolution in an impulsively started jet using digital image particle velocimetry and continuous wavelet analysis. Meas. Sci. Technol. **12**:1413-1421

[19] Duraisamy K, Ramasamy M, Baeder JD, Leishman JG (2006) Computational/Experimental Study of Hovering Rotor Tip Vortex Formation. Proc. 62nd Annual Forum of the American Helicopter Society, Phoenix, USA

[20] G.H. Vatistas, V. Kozel, W.C. Mih (1991) A simpler model for concentrated vortices. Exp. in Fluids **11**: 73-76

[21] C. Schram, M.L. Riethmuller (2001) Vortex ring evolution in an impulsively started jet using digital image particle velocimetry and continuous wavelet analysis. Measurement Science and Technology **12**: 1413-1421